Journal of Alloys and Compounds 504 (2010) 37–44

Contents lists available at ScienceDirect

Journal of Alloys and Compounds

journal homepage: www.elsevier.com/locate/jallcom

Morphological evolution of Ag_2Te precipitates in thermoelectric PbTe

J.L. Lensch-Falk*, J.D. Sugar, M.A. Hekmaty, D.L. Medlin

Materials Physics Department, Sandia National Laboratories, Livermore, CA, 94550, United States

ARTICLE INFO

Article history:
Received 16 March 2010
Received in revised form 28 April 2010
Accepted 5 May 2010
Available online 8 June 2010

Keywords:
Thermoelectric materials
Precipitation
Microstructure
Transmission electron microscopy
Atom probe tomography

ABSTRACT

The precipitation of Ag_2Te in a PbTe matrix is investigated using electron microscopy and atom probe tomography. We observe the formation of oriented nanoscale Ag_2Te precipitates in PbTe. These precipitates initially form as coherent spherical nanoparticles and evolve into flattened semi-coherent disks during coarsening. This change in morphology is consistent with equilibrium shape theory for coherently strained precipitates. Upon annealing at elevated temperatures these precipitates eventually revert to an equiaxed morphology. We suggest this shape change occurs once the precipitates grow beyond a critical size, making it favorable to relieve the elastic coherency strains by forming interfacial misfit dislocations. These investigations of the shape and coherency of Ag_2Te precipitates in PbTe should prove useful in the design of nanostructured thermoelectric materials.

1. Introduction

Nanostructuring of thermoelectric materials is expected to enhance thermoelectric properties by reducing the thermal conductivity and improving the power factor from that of homogeneous bulk materials [1–4]. Theoretical predictions [5–7] and experimental observations [8–10] of enhanced properties in nanostructured materials have motivated interest in employing solid-state reactions to tailor the microstructure in bulk thermoelectric materials for enhanced properties [3,8,11–15]. Knowledge of the evolution of precipitate size and morphology with time at elevated temperatures is important for understanding and predicting the thermal stability and thermoelectric properties of thermoelectric materials.

In particular, interest in Ag-rich phases embedded within rocksalt tellurides has emerged in recent years. For instance, Ag_2Te precipitates have been analyzed in $AgSbTe_2$ [13,16] and in the closely related $Cu_xAg_{3-x}SbSeTe_2$ system [17]. The LAST system (lead–antimony–silver–telluride), which has a general composition of the form $AgPb_mSbTe_{2+m}$ has received much attention due to the high ZT values reported [8,18,19]. It has been suggested that embedded Sb-rich and/or Ag-rich nanoprecipitates, including Ag_2Te nanoprecipitates, lead to the enhanced properties in LAST thermoelectric materials [8,18,20,21]. However, the parameters that control precipitate morphology and stability are poorly understood in these systems. To study the fundamental mechanisms of Ag_2Te precipitation in a system of less complexity than the quaternary LAST system, we have focused on the ternary Pb–Ag–Te system. This system is also of interest as Ag is often used as a dopant in PbTe for thermoelectric applications [22–25].

Fig. 1 illustrates the quasi-binary PbTe–Ag_2Te section of the ternary Ag–Pb–Te equilibrium phase diagram [26,27]. Precipitation of Ag_2Te in PbTe is thermodynamically favored below the eutectic temperature. PbTe has a cubic rocksalt crystal structure [28] (space group: $Fm\bar{3}m$; $a = 6.46$ Å at room temperature) with Pb atoms occupying one sublattice and Te atoms occupying an equivalent sublattice offset by [1/2, 1/2, 1/2]a, as shown in Fig. 1b. Ag_2Te exhibits three known phases [29]. The high-temperature BCC γ-Ag_2Te phase is stable at temperatures between 800 and 959 °C, while the α-Ag_2Te phase is thermodynamically favored at the temperatures generally used for operation of PbTe thermoelectric devices and for heat treatments of PbTe–Ag_2Te materials (140–694 °C). The α phase has an FCC crystal structure [30] (space group: $Fm\bar{3}m$; a = 6.63 Å at 400 °C; Fig. 1c) with the Te atoms on the FCC sites, half of the Ag atoms occupying the [1/4, 1/4, 1/4]a positions, and the remaining Ag occupying interstitial sites. Below 140 °C α-Ag_2Te transforms to the monoclinic phase, β-Ag_2Te (space group: $P2_1/c$; $a = 8.09$ Å, $b = 4.48$ Å, $c = 8.96$ Å, $\beta = 123.2°$), in which the Te and Ag atoms are slightly shifted from their positions in the FCC structure (Fig. 1d) [29,31,32].

In general, the morphology of precipitates in a matrix is dependent upon the crystal structures of the two phases, their associated coherency and misfit, the matrix/precipitate interfacial energy, and the elastic moduli. Because of their closely related crystal

* Corresponding author. Tel.: +1 925 294 3544; fax: +1 925 294 3231.
E-mail addresses: jllensc@sandia.gov (J.L. Lensch-Falk), jdsugar@sandia.gov (J.D. Sugar), mabanke@sandia.gov (M.A. Hekmaty), dlmedli@sandia.gov (D.L. Medlin).

0925-8388/$ – see front matter © 2010 Elsevier B.V. All rights reserved.
doi:10.1016/j.jallcom.2010.05.054

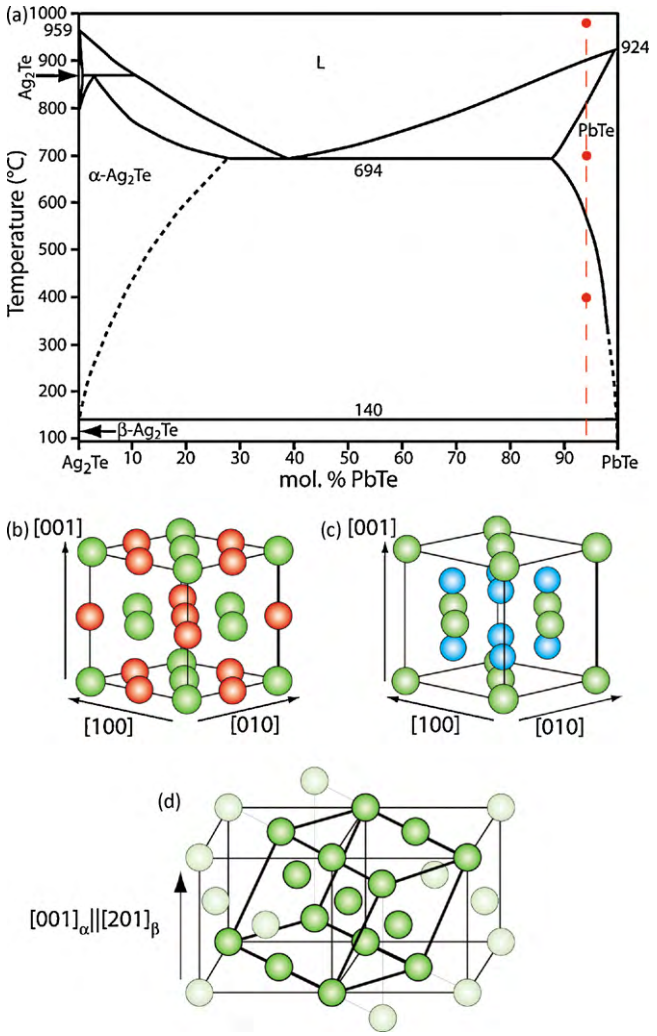

Fig. 1. (a) Quasi-binary Ag_2Te-PbTe phase diagram with composition indicated by the dashed line and heat treatment temperatures by dots. The crystal structures of PbTe (b) and α-Ag_2Te (c) are shown with Te atoms in green, Pb in red, and Ag in blue. In the α-Ag_2Te structure only the Ag atoms on the tetrahedral sites are shown. The remaining half of the Ag atoms occupy interstitial sites. (d) The relationship between the cubic α-Ag_2Te and monoclinic β-Ag_2Te using the Te sublattice is illustrated; the monoclinic [2 0 1] is oriented parallel to the cubic [0 0 1] as described by Manolikas [29]. The Te atoms used to make the monoclinic unit cell are shown in bright green while those not used are dulled. (For interpretation of the references to colour in this figure legend, the reader is referred to the web version of the article.)

structures, the question arises as to whether the Ag_2Te precipitates are aligned with respect to the PbTe matrix and, if so, what are the implications of the resulting interfacial coherency on the precipitate evolution. We address this question in this study by investigating precipitation of Ag_2Te in a PbTe matrix using electron microscopy and atom probe tomography (APT). We analyze the coarsening, morphology, and crystallographic alignment of these precipitates and relate these observations to equilibrium shape theory.

2. Materials and methods

2.1. Synthesis

An ingot having the composition $(Ag_2Te)_{0.05}(PbTe)_{0.95}$ was prepared using Ag_2Te (Strem Chemicals, 99.99%) and PbTe (Sigma Aldrich, 99.998%) as stock materials. We chose this composition because it is within the single-phase region above 600 °C and is in the two-phase Ag_2Te + PbTe region at lower temperatures such that phase separation to occur through solid-state precipitation (Fig. 1). Ag_2Te and PbTe pieces were mixed in appropriate fractions and placed in a quartz tube. This tube was evacuated to less than 10^{-7} Torr before it was sealed while actively pumping. The contents of the sealed ampoule were melted at 975 °C for 2 h and then cooled at 25 °C/h to 700 °C. The ingot was held at this temperature, which is in the single-phase PbTe region of the phase diagram, for 75 h to allow it to equilibrate. Following this step, the ingot was quenched into an iced-brine solution to bring it to room temperature. Pieces of the quenched ingot were then annealed in sealed and evacuated ampoules for 1–24 h at 400 °C to precipitate Ag_2Te within the PbTe matrix.

2.2. Characterization

Powder X-ray diffraction (XRD) was utilized to determine the phases present in the heat treated ingot. The microstructure was analyzed using optical microscopy, scanning electron microscopy (SEM, JEOL 840), and transmission electron microscopy (TEM, 200 kV JEOL 2010F). TEM and energy dispersive x-ray spectroscopy (EDS, Oxford Inc.) were employed for identification and imaging of the Ag-rich precipitates, while electron diffraction was utilized to determine the crystallographic orientation of these precipitates in the matrix. High-resolution (HRTEM) imaging was conducted using a JEOL 4000EX TEM operated at 400 kV. Further analysis of the matrix and precipitate compositions was conducted using atom probe tomography (APT, Imago LEAP 3000).

APT provides atomic scale spatial resolution with very good atomic specificity and is particularly useful for measuring the composition of embedded precipitates [33,34]. The technique combines field evaporation of individual ions with a time-of-flight mass spectrometer to provide composition in three dimensions. The controlled field evaporation of PbTe-based alloys is possible using voltages of 1500–7000 V with applied pulses of 15% of the standing voltage at temperatures less than 40 K. Three-dimensional reconstructions were formed from the collected data (position and time-of-flight) using the IVAS software provided by Imago Scientific Instruments.

Specimens for analysis by TEM were prepared by mechanical thinning and dimpling (Gatan 656 Dimple Grinder) followed by Ar^+ ion milling (Fischione 1010) at 140–160 K. We have found that rigorous control of the temperature and duration of the ion milling step is critical to achieving high quality samples and avoiding ion milling artifacts that could erroneously be interpreted as nanoscale precipitates. Further details regarding TEM specimen preparation are provided in Appendix A. Needle-like specimens with tip diameters of less than 100 nm are necessary to conduct APT studies. To achieve this geometry we used an approach similar to that described by Thompson et al. [35] and Miller et al. [36]. Specifically, selected regions were lifted out of the ingot, mounted on silicon microposts, and annularly milled to the desired geometry using a FEI Nova600 Dual beam FIB equipped with an "Xtreme Access" micro-manipulator.

3. Results and discussion

3.1. Morphology and coarsening of Ag_2Te precipitates

Analysis of the ingot using optical microscopy, SEM, and EDS indicated that the microstructure and composition were homogeneous across the quenched ingot. Precipitates were observed in all samples and confirmed to be monoclinic β-Ag_2Te via XRD as shown in Fig. 2. The Ag_2Te precipitates observed via SEM and TEM have a plate-like geometry that is elongated parallel with ⟨0 0 1⟩ directions in the PbTe matrix as shown in Fig. 3. The crystallographic orientation relationship and origins of the precipitate morphology are discussed in greater detail below.

In the sample quenched from the single-phase region, a high density of small precipitates was observed as shown in Fig. 2b. The presence of precipitates in this specimen was unexpected and is discussed in further detail in the following section. We measured the shape and number density of the Ag_2Te precipitates as a function of annealing using a statistical analysis of SEM images (Fig. 2b and c) in which precipitates were measured in multiple differently oriented grains. The sizes of the precipitates measured by SEM were generally greater than the minimum resolution of the SEM and are consistent with those measured using TEM suggesting that the measurements of the disc-shaped precipitates by SEM were reasonably accurate. The precipitates were found to coarsen upon annealing at 400 °C as indicated by an increase in precipitate size (Fig. 5a–c) and a decrease in number density (Fig. 4a). We also observe that the areal fraction is observed to be constant with time confirming that the material is in the coarsening regime (Fig. 4b). The experimental volume fraction, V_V, was calculated from the measured area fraction, A_A, using a stereological relationship, $V_V = KA_A$, in which K (≈0.35 for the data analyzed here) is based on

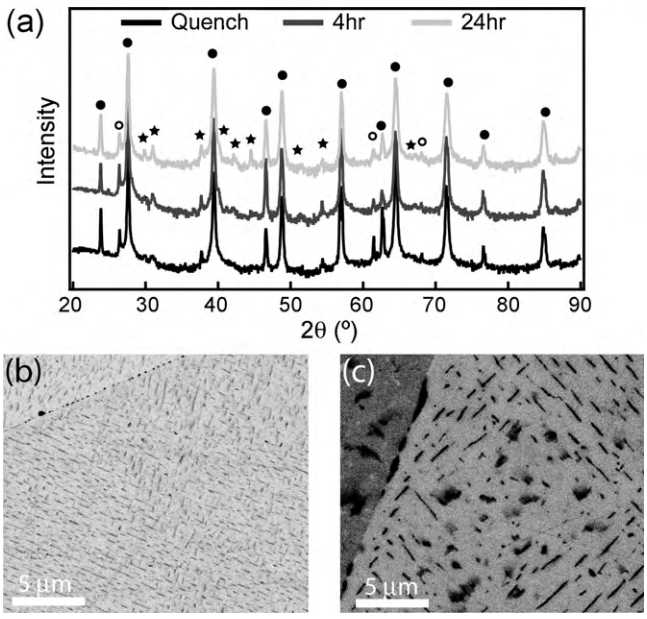

Fig. 2. (a) XRD θ–2θ scans for samples quenched and annealed for 4 and 24 h in the region of two-phase equilibrium. Filled circles are PbTe, stars are Ag_2Te, and open circles represent peaks associated with oxide phases including Pb_3O_4 and SiO_2. The intensity is plotted on a logarithmic scale to make the minority phase peaks more visible. (b) SEM image of the quenched sample. (c) SEM image of the sample annealed for 24 h at 400 °C.

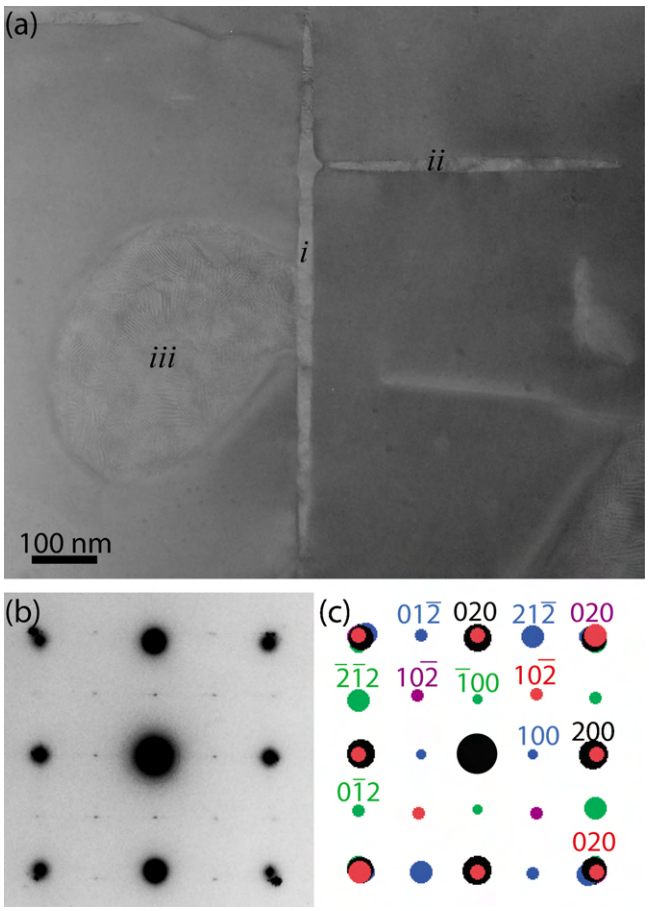

Fig. 3. (a) TEM image and (b) electron diffraction pattern for an [0 0 1] PbTe zone from a sample quenched from 700 °C indicating the observed precipitates are Ag_2Te and are aligned to the PbTe matrix. Three disk-shaped precipitates oriented to the PbTe {1 0 0} planes are shown in (a). The precipitates labeled *i* and *ii* are oriented with the flat edge parallel to the $(1\,0\,0)_{PbTe}$ and $(0\,1\,0)_{PbTe}$, respectively. The precipitate labeled *iii* is oriented with the flat (broad) edge parallel to the $(0\,0\,1)_{PbTe}$. (c) The expected electron diffraction pattern for PbTe (black) and the four distinct β-Ag_2Te variants with respect to the PbTe lattice are shown. The spots corresponding to the $[0\,0\,1](2\,0\,0)_{PbTe}||[0\,2\,1](1\,1\,\bar{2})_{\beta\text{-}Ag_2Te}$, $[0\,0\,1](0\,2\,0)_{PbTe}||[0\,2\,1](1\,1\,\bar{2})_{\beta\text{-}Ag_2Te}$, $[0\,0\,1](2\,0\,0)_{PbTe}||[\bar{2}\,0\,1](1\,1\,\bar{2})_{\beta\text{-}Ag_2Te}$, and $[0\,0\,1](0\,2\,0)_{PbTe}||[\bar{2}\,0\,1](1\,1\,\bar{2})_{\beta\text{-}Ag_2Te}$ variants are shown in green, blue, red, and purple respectively. (For interpretation of the references to colour in this figure legend, the reader is referred to the web version of the article.)

the sampling depth in the SEM (~700 nm for 15 keV electrons in PbTe), and the average aspect ratio and average size of the precipitates in a sample [37]. This gives a calculated experimental volume fraction of ~3.5%, whereas the expected volume fraction based on the phase diagram is ~3.9%. Given the uncertainties present in the phase boundaries in the phase diagram, these values are consistent with one another.

The increase in precipitate size is rapid at short anneal times, but slows with increased anneal time. Similarly, while the measured areal precipitate number density decreases initially, it remains nearly unchanged between the 4 and 24 h precipitation anneals.

Histograms of the ratio of precipitate width-to-length were utilized to examine the evolution of the precipitate morphology. The average width-to-length ratio is approximately 0.4 for the quenched sample and for those annealed for 4 and 24 h. While the average aspect ratio remains nearly constant over this time period, the histograms (Fig. 5d–f) show that the spread in the distribution of precipitate width-to-length ratio is reduced with increased anneal time as a result of a reduction in the number of nearly equiaxed precipitates. It should be noted that one may expect a bimodal width-to-length ratio for a system with plate-like precipitates aligned to cubic ⟨0 0 1⟩ directions, with one peak corresponding to those that appear needle-like (thin edge perpendicular to viewing direction) and another to those that are flat (wide edge perpendicular to viewing direction) such as is observed here. However, because SEM is sensitive only to the near-surface region and the probability of intersecting thin precipitates aligned parallel with the surface is low, we measure only a single peak in the distribution.

3.2. Ag_2Te precipitation during quench

In addition to the plate-like precipitates described above, TEM shows a second group of much smaller, nanoscale precipitates in all of the samples (Fig. 6b). These precipitates are spherical and have diameters less than ~15 nm, with an average diameter of ~6 nm. We confirmed that these precipitates are Ag-rich using EDS in STEM mode with a 1.6 nm electron beam probe. However, STEM-EDS is unable to determine the composition of these precipitates since they are fully embedded within the PbTe matrix. To resolve this problem, we employed APT to determine the composition of the precipitates (Fig. 6). Details pertaining to this analysis can be found in Appendix B. APT analysis of mass spectra (Fig. 6d and e) taken from within these precipitates in the quenched sample indicates the average composition is 59.7 ± 0.9 at.% Ag, 39.4 ± 1.8 at.% Te, and 2.9 ± 0.2 at.% Pb, which approaches the composition expected for Ag_2Te. The measured Pb content is not surprising as a small but finite amount of PbTe is expected to be soluble within Ag_2Te [26,27]. Based on the limited volumes sampled by APT and HRTEM, we estimate the number density of these nanoscale precipitates is on the order of $10^4/\mu m^3$ for all of the samples.

As mentioned above, the observation of precipitates in the sample quenched from the single-phase region was unexpected. Here we consider whether the Ag_2Te precipitates observed would be formed at 700 °C or during cooling. As both experimental works describing the Ag_2Te–PbTe pseudo-binary equilibrium phase dia-

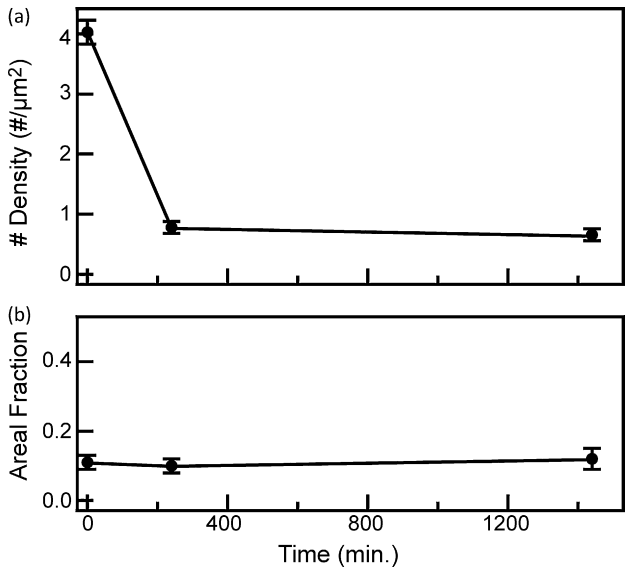

Fig. 4. (a) Areal precipitate number density vs. time. (b) Precipitate area fraction vs. anneal time indicating that the material is in the coarsening regime. This data is collected from SEM images.

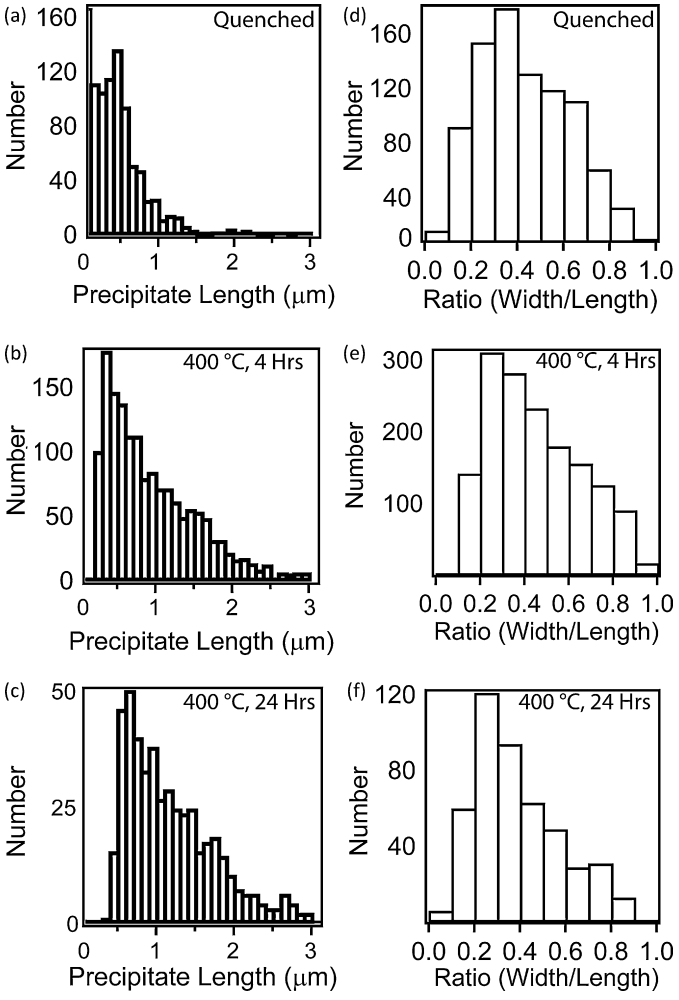

Fig. 5. The distribution of lengths of Ag_2Te precipitates is shown for the (a) quenched, (b) 4 h, 400 °C and (c) 24 h, 400 °C annealed samples. The distribution of width-to-length ratio for these precipitates is shown for the (d) quenched, (e) 4 h, and (f) 24 h samples. This data is collected from SEM images.

gram [26,27] are in agreement on the solubility of Ag_2Te in PbTe at 700 °C, we are confident that the high-temperature solution anneal was indeed in the single-phase region of the phase diagram. Moreover, the degree of coarsening observed at 400 °C suggests that much larger particles would be expected if precipitation had occurred at the higher temperature of 700 °C.

Instead, it is possible that as a result of the high mobility of Ag in PbTe the precipitates are able to form at lower temperatures during the brief period of the quench. Based on calculations of expected cooling rates for cylindrical telluride ingots conducted by Ikeda, it is reasonable to assume that it will take 30–60 s for the center of the ingot to cool to room temperature [38], which should be sufficient for the formation of Ag_2Te precipitates at moderate temperatures. This calculation, which is based on the thermal conductivity of the ingot and quartz, should be valid for the material quenched from the single-phase region as the ingot was in direct contact with the quartz wall. Furthermore, in practice, the ingot was found to cool sufficiently for handling outside the quartz tube within a few minutes after removal from the furnace (the time required to remove the material from the quartz tube). Ag is a fast diffuser in PbSe ($D_0 = 7.4 \times 10^{-8}$ m^2/s, $E_a = 0.35$ eV, 400–850 °C) where the diffusion length, $L \approx \sqrt{Dt}$, is 20 m in 1 s (~180 μm in 1 min) at 550 °C (the solvus temperature for 5 mol.% Ag_2Te in PbTe) [39]. Ag diffusion is expected to be faster in PbTe because it has the same crystal structure with a larger lattice constant and Ag diffusion should occur via interstitial sites [40]. Thus, due to the high diffusivity of Ag and relatively slow cooling rates, it is reasonable that the nanoscale precipitates form due to solute rejection occurring during this brief cool-down period.

It is also likely that the nanoscale Ag_2Te precipitates observed in samples annealed at 400 °C form during the quench to room temperature. The rapid formation of nanoscale precipitates during cooling is made possible by the high mobility of Ag in the rocksalt structure, the large changes in Ag_2Te solubility with temperature, and the slower cooling rates due to the poorer contact of the annealed material with the quartz tube walls. The slope of the solvus curve in the published phase diagram [26,27] and the analysis of the matrix composition at room temperature by APT support the formation of nanoscale precipitates during cooling. At 400 °C the phase diagram predicts ~1 mol.% Ag_2Te to be soluble in PbTe, but compositional analysis by APT indicates that less than 0.05 mol.% Ag_2Te is present in the PbTe matrix at room temperature. This result is consistent with the reduction in Ag_2Te solubility in PbTe at decreased temperatures and our hypothesis that additional phase separation occurs during the quench. We note that the presence of these nanoscale features at room temperature does not guarantee their existence at elevated temperature where the increased thermodynamic solubility of Ag_2Te in the matrix and the high mobility of Ag should allow the Ag_2Te nanoparticles to dissolve back into the matrix.

3.3. Orientation relationship and coherency

We investigated the crystallographic alignment of the precipitates to better understand the interfacial coherency and its relationship to precipitate morphology. Electron diffraction and HRTEM measurements show that the Ag_2Te precipitates are crystallographically aligned with the PbTe matrix. The diffraction pattern in Fig. 3, which is aligned along a [001] zone axis in PbTe, shows spots corresponding to the monoclinic β-Ag_2Te phase. Four unique orientation variants are observed in this pattern: $[001](200)_{PbTe}||[021](11\bar{2})_{\beta\text{-}Ag_2Te}$, $[001](020)_{PbTe}||[021](11\bar{2})_{\beta\text{-}Ag_2Te}$, $[001](200)_{PbTe}||[\bar{2}0\bar{1}](11\bar{2})_{\beta\text{-}Ag_2Te}$, and $[001](020)_{PbTe}||[\bar{2}0\bar{1}](11\bar{2})_{\beta\text{-}Ag_2Te}$. These orientation variants, which are equivalent to those reported pre-

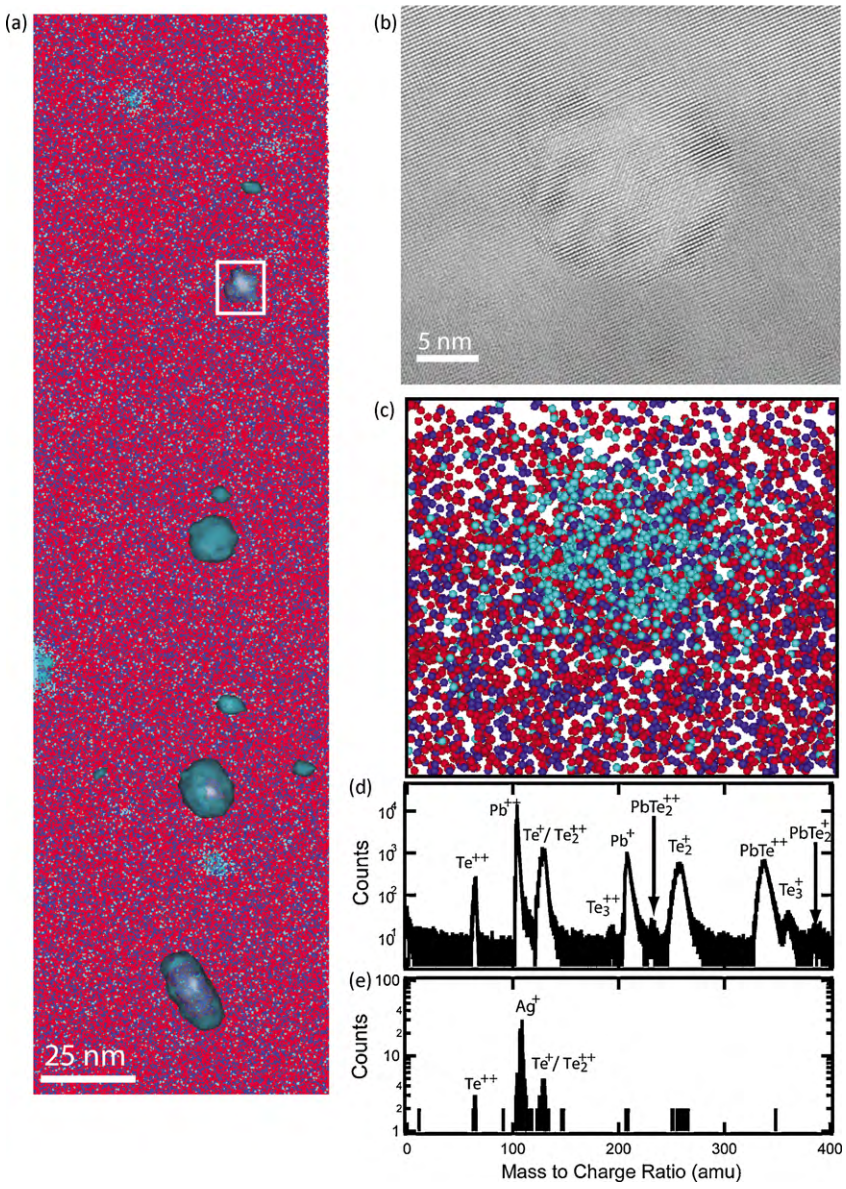

Fig. 6. (a) 3D APT reconstruction of a PbTe/Ag_2Te specimen that was quenched from 700 °C with each detected ion represented by a point. Pb is shown in red, Te in blue, and Ag in teal. To emphasize the precipitates, a 20% Ag iso-concentration surface is shown in dark teal and only 20% of the Pb and Te ions are shown. (b) HRTEM image of a nanoscale Ag_2Te precipitate. (c) A magnified slice (2 nm thick) of the reconstruction shown in (a) highlights the presence of Ag rich precipitates. Mass spectra from the PbTe matrix (d) and from within the precipitate (e). (For interpretation of the references to colour in this figure legend, the reader is referred to the web version of the article.)

viously between the α- and β-forms of Ag_2Te[29] and for β-Ag_2Te in rocksalt structured $AgSbTe_2$[13], align the Te-sublattices in both the PbTe and Ag_2Te (Fig. 1).

The alignment of planes across the interface is also clear in the HRTEM images of precipitates shown in Fig. 7. Here, we observe both fully coherent precipitates, with no interfacial dislocations, as well as larger, semi-coherent precipitates, as indicated by the presence of dislocations. These precipitates form with multiple monoclinic orientation variants. The orientation relationship between the monoclinic and cubic crystal structures is such that the {0 0 1} planes in the cubic crystal are parallel to (2 0 0), (1 $\bar{1}$ $\bar{2}$), and (1 1 $\bar{2}$) planes in the monoclinic crystal. Compared to the {100} interplanar spacing for the cubic α-Ag_2Te structure, the monoclinic structure has a larger interplanar spacing for (2 0 0) planes (+4.46%), but smaller spacing for {1 1 $\bar{2}$} planes (−2.04%). When the system is viewed along any ⟨0 0 1⟩ PbTe zone, four distinguishable variants, which are rotated by ≈90° with respect to each other, are visible as shown in Fig. 3. Two variants will arise where the lattice spacing is smaller than that of PbTe for planes parallel to the (2 0 0) and (0 2 0) PbTe planes (indexed in red and purple in Fig. 3c). Additionally, two more variants will have one set of planes that are parallel to the (2 0 0) PbTe planes with smaller lattice spacing and an orthogonal set of planes that are parallel to the (0 2 0) PbTe planes with larger lattice spacing than the equivalent PbTe planes (indexed in green and blue in Fig. 3c). It is likely that the specific arrangement of variants that form within a given precipitate minimizes the elastic strain energy of the system for large precipitates.

The transformation from the high-temperature cubic α-Ag_2Te phase to the low temperature monoclinic β-Ag_2Te phase occurs through a displacive mechanism requiring only small, local atomic shifts to accomplish the transformation [29,41]. Thus, while the above observations are of Ag_2Te in its low-temperature, monoclinic form, they provide insight concerning the precipitate orientation at the synthesis temperature, for which the cubic α-Ag_2Te phase is stable. In particular, the multiple variants observed in the low-symmetry monoclinic β-Ag_2Te phase are all derived from a single

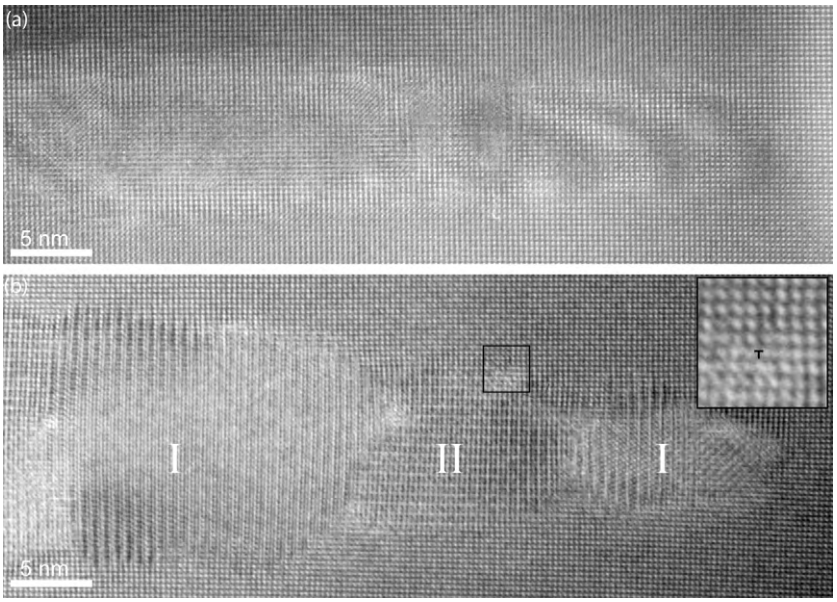

Fig. 7. HRTEM images oriented on the [0 0 1] PbTe zone axis (a) showing a fully coherent Ag_2Te precipitate in which no misfit dislocations are observed and (b) showing a semi-coherent Ag_2Te precipitate with multiple monoclinic variants (labeled I and II). The inset is a magnification of the boxed area highlighting a misfit dislocation in the precipitate. Images were taken from a specimen that was quenched from 700 °C and are representative of (a) coherent and (b) semi-coherent precipitates observed in all specimens using HRTEM.

variant in the higher symmetry, cubic α-Ag_2Te phase [29]. As we have shown previously for the case of Ag_2Te in $AgSbTe_2$ [13], the observed orientation of the β-Ag_2Te allows us to infer that the high-temperature cubic α-Ag_2Te phase is oriented in a simple cube-on-cube relationship with the PbTe matrix. Assuming this alignment, and using thermal expansion and high-temperature lattice parameter data for PbTe [42] and Ag_2Te [41], we estimate a lattice misfit $((a_{Ag_2Te} - a_{PbTe})/a_{PbTe})$ of +1.8% for α-Ag_2Te with respect to PbTe at the synthesis temperature (400 °C).

The strong orientation relationship and coherent/semi-coherent interfaces observed in the PbTe/Ag_2Te system are a result of the close lattice match and similarities in the crystal structures of the two phases. As we discuss next, the coherency and transition to semi-coherency have implications on the morphological evolution of the Ag_2Te precipitates.

3.4. Discussion of precipitate evolution

The morphology of embedded crystalline precipitates is typically controlled by the interplay between elastic coherency strains, which arise due to misfit across the precipitate/matrix interface, and the interfacial energy, which, in general, depends anisotropically on the local orientation of the interface. At elevated temperatures, we expect the interfacial energy anisotropy to reflect the cubic symmetry of the crystal structures in the α-Ag_2Te precipitate and PbTe matrix phases; thus it is unlikely that interfacial energy anisotropy could explain the highly elongated lenticular morphologies that we observe. On the other hand, it is known that coherently strained precipitates can adopt anisotropic structures and/or morphologies to minimize the total energy of the system [43–45]. In particular, Nabarro showed that an elastically strained precipitate can reduce its strain energy by forming as a disk rather than a sphere [46]. In recent years, this concept has been extended to account for both interfacial energy and elastic strain energy [47,48]. Based on these results, one expects a misfitting precipitate to grow initially as a spherical particle to minimize interfacial energy at small sizes. However, as the precipitate grows, and the volume increases with respect to the interfacial area, the effects of elastic strain will dominate, leading to a convex, disk-shaped precipitate. The critical size, l_c, at which this transition occurs is controlled by the balance between interfacial energy and elastic strain energy and is given by Thompson and Voorhees [48] as $l_c \approx 5.35\sigma/\varepsilon^2 c_{44}$, where ε is the misfit strain, σ the interfacial energy, and C_{44} the shear modulus. Because the elastic moduli for Ag_2Te and interfacial energies for Ag_2Te/PbTe are unknown, an exact value cannot be calculated. However, using 1.8–2.2% misfit and by assuming values for the elastic moduli similar to that for PbTe [49] and other chalcogenides [50] (15–35 GPa) and interfacial energies consistent with coherent interfaces [51–53] (20–500 mJ/m^2), critical sizes of ≈5–500 nm would be expected. Elastic anisotropy breaks the symmetry in a system in which both the precipitate and matrix are cubic, causing precipitates to flatten along an elastically soft direction.

The observations we have presented are consistent, at least qualitatively, with the notion that coherency strains control the precipitate morphology. In particular, the very smallest Ag_2Te nanoprecipitates, which we believe form during the quench from 400 °C, are spherical. In contrast, the larger precipitates, with radii of approximately 15 nm, form in a disk-shaped morphology, as predicted by theory. Further evidence is found in the decreased number of equiaxed precipitates with increased anneal time as observed in the distributions of precipitate width-to-length ratio (Fig. 5).

For sufficiently large precipitates it becomes energetically favorable to reduce the coherency strain energy by forming misfit dislocations, creating a semi-coherent interface [54]. Since the Ag_2Te precipitates form in a lenticular morphology, we can estimate this critical thickness using the elastic solution for an embedded, biaxially strained layer [55], which should be reasonable in the middle of an anisotropic ellipsoidal precipitate. The critical thickness, h, is given by:

$$h = \frac{\lambda}{8\pi}\left[\ln\left(\frac{2\pi h}{\lambda}\sinh\left(\frac{2\pi h}{\lambda}\right)\right) - \ln\left(\cosh\left(\frac{2\pi b}{\lambda}\right) - 1\right)\right] \quad \text{where } \lambda = \frac{b}{\varepsilon}.$$

In the Ag_2Te/PbTe system we assume that the Burgers vector, b, is along the $\langle 0\,0\,2\rangle_{PbTe}$ and has a value approximately that of the plane spacing for $\{0\,0\,2\}_{PbTe}$ (≈0.325 nm at 400 °C). The lattice misfit, ε, is taken to be 0.018, which is the lattice mismatch between α-Ag_2Te and PbTe at 400 °C. An iterative numerical method was

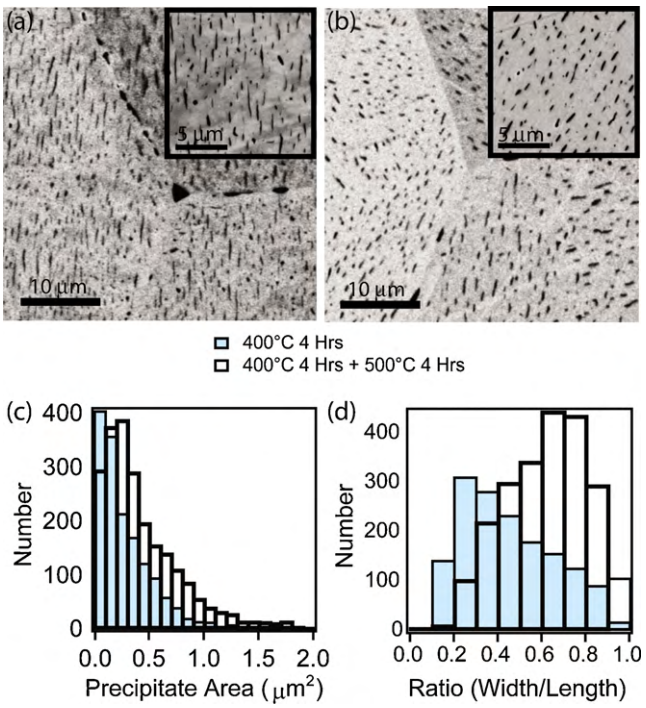

Fig. 8. SEM images of (a) a specimen annealed for 4 h at 400 °C and (b) a specimen annealed for 4 h at 400 °C then 4 h at 500 °C. Insets are higher magnification images. Histograms of precipitate area (c), and width-to-length ratio (d) are shown for both of these samples.

used to solve this equation for the critical thickness giving a value of ≈4.5 nm. Similar results (within 5%) are obtained using the Matthews–Blakeslee expression [56]. Careful analysis of precipitate coherency and size for the Ag_2Te precipitates considered here using HRTEM data suggests that the transition from a coherent to semi-coherent state occurs at thicknesses of ∼12–14 nm, which is on the same order of magnitude as the value predicted by the biaxially strained layer model. Considering that approximations of the lattice constants were made based on thermal expansion coefficients which affect both b and ε, the calculated value is quite close to the observed critical thickness.

Furthermore, we would expect that precipitates could persist in a metastable coherent state beyond this critical thickness if kinetics limit the formation of misfit dislocations, delaying the accumulation of sufficient quantities of interfacial misfit dislocations to fully relieve the coherency strains. However, once these coherency strains are relieved, the energetic preference for a lenticular morphology should vanish, and the precipitates should evolve toward a more equiaxed shape that minimizes the interfacial energy.

We tested this hypothesis by annealing a sample that had been annealed initially for 4 h at 400 °C for an additional 4 h at 500 °C. We chose this temperature since it lies below the solvus line, ensuring that material would remain in the region of two-phase equilibrium. (Note: at 500 °C, the misfit strain increases slightly to about 2%.) As shown in Fig. 8, this second anneal leads to continued coarsening of the precipitates. This growth is accompanied by a marked shift in the distribution of width-to-length ratios toward values approaching unity, demonstrating that the precipitates do evolve toward a more isotropic morphology.

4. Conclusions

In summary, our investigation of the precipitation of Ag_2Te in PbTe reveals an evolution in precipitate size, morphology, and coherency. Initially, spherical coherent nanoscale Ag_2Te precipitates nucleate by solid-state phase separation both at elevated temperatures and during cooling. At larger sizes, Ag_2Te precipitates are observed to be ellipsoidal disks which are aligned to the PbTe matrix with coarsening. This morphological evolution is consistent with competition between elastic misfit energy and interfacial energies at the matrix/precipitate interface. However, for sufficiently large precipitates, relief of the coherency strains allows a more isotropic morphology to develop. The orientation relationship between the monoclinic β-Ag_2Te and PbTe is consistent with that previously reported for Ag_2Te in other rocksalt structured tellurides, suggesting that this relationship may be generally expected due to the alignment of the Te sublattices in the two crystals.

In multiphase, nanostructured thermoelectric materials, the evolution of precipitate size, morphology, and number density is expected to affect thermoelectric transport properties. The present results should therefore help in understanding and predicting the behavior of Ag_2Te precipitates in rocksalt structured telluride thermoelectrics such as LAST and $AgSbTe_2$. More generally, we expect careful consideration of the crystal structures, lattice misfit, interface structure, and their role in precipitate evolution to be important for the development of nanostructured multiphase thermoelectric materials.

Acknowledgements

The authors would like to thank Andy Gardea, Jeff Chames, and Ryan Nishimoto for metallurgical preparation and imaging of SEM specimens, Nick Teslich for his assistance in preparation of specimens for APT at Lawrence Livermore National Laboratories, and Drs. Norm Bartelt, Steve Goods, Rick Karnesky, and Nancy Yang for useful discussions and suggestions. Sandia is a multiprogram laboratory operated by Sandia Corporation, a Lockheed-Martin Company, for the United States Department of Energy, National Nuclear Security Administration under Contract DE-AC04-94AL85000. Support was provided in part by the US Department of Energy, Office of Basic Energy Sciences, Division of Materials Sciences.

Appendix A. TEM specimen preparation

In the course of preparing specimens for TEM for this work we found that the ion milling step must be carefully controlled to limit damage to PbTe-based materials. PbTe specimens containing no silver that were prepared by ion milling at or near room temperature or for extended times (many hours) exhibited extensive damage, which appears as nanoscale features in the material as observed by TEM (Fig. A1). These artifacts complicate the interpretation of TEM images and associated analysis of $(PbTe)_{1-x}(Ag_2Te)_x$ alloys, since this material contains nanoscale precipitates of the same size as the damage observed in pure PbTe due to ion milling. We have found that cooling specimens to cryogenic temperatures (140–160 K) in the ion milling stage greatly limits the extent of the damage, as can be seen in Fig. A1. Additionally, we find that shorter ion milling times and milling at a low angle (6°) and low energy (1.5 kV, 3 mA) as a final step further reduce the extent of ion milling damage.

Appendix B. Analysis of APT mass spectrum and reconstruction

In alloy specimens it is important to ensure that appropriate evaporation conditions are utilized during the atom probe tomography (APT) experiments. PbTe and $(PbTe)_{0.95}(Ag_2Te)_{0.05}$ specimens were analyzed via APT at various pulse fractions (frac-

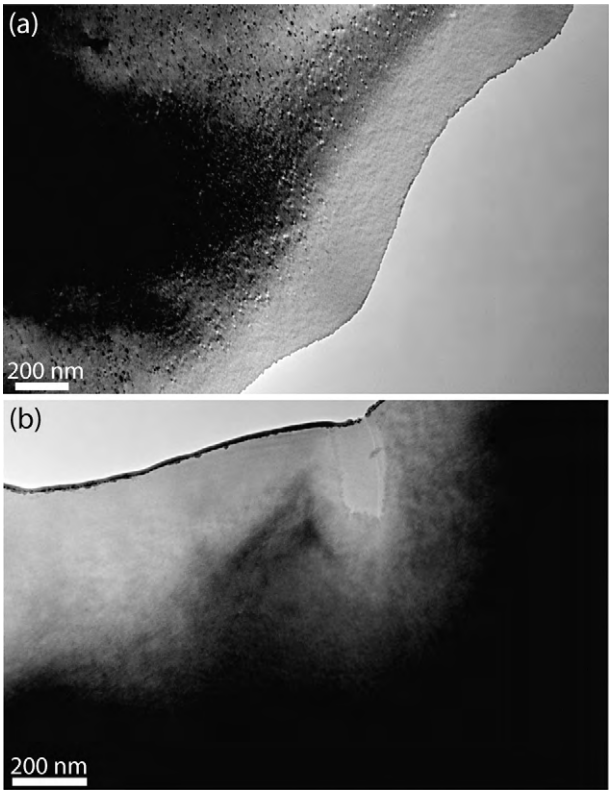

Fig. A1. TEM images from PbTe samples demonstrating the effect of sample temperature during ion milling. Specimens processed at room temperature (a) show many nanoscale features that specimens processed at less than 160 K (b) do not exhibit.

tion of total standing voltage). The associated mass spectra were analyzed to ensure that the data presented here was collected at conditions which avoid preferential evaporation.

Analysis of a mass spectrum provides the composition of the material. In PbTe samples the peaks observed included Te^{++}, Pb^{++}, $Te^{+}/Te_2{}^{++}$, $Te_3{}^{++}$, Pb^{+}, $PbTe_2{}^{++}$, $Te_2{}^{+}$, $PbTe^{++}$, $Te_3{}^{+}$, and $PbTe_2{}^{+}$. In the Ag-containing samples, the Ag^{+} peaks were the only peaks associated with Ag. Adding up the total counts under each peak (above background) and considering the identity of that peak allows the atomic fractions of each elemental species to be determined. In the case of telluride-based materials, this analysis is complicated by the overlap of the $Te^{+}/Te_2{}^{++}$ peaks. To separate out the two peak signatures and to appropriately count the Te atoms, multi-peak fitting in Igor Pro (WaveMetrics) was utilized with the expected peak positions and mass abundances of each of the 8 Te^{+} peaks and 18 $Te_2{}^{++}$ peaks used as initial inputs. Similar fitting procedures were used to measure the Ag^{+} peaks, which fall on the tail of the Pb^{++} peak.

Further analysis of the atom probe tomography data is conducted using a software package, IVAS (Imago Scientific Instruments), which utilizes the collected ion position data, time-of-flight and the assigned peak identities in the mass spectra to form a 3D reconstruction. For this reconstruction, it is important to ensure that the dimensions are consistent with the specimen. We measured both the tip diameter and shank angle before analysis. Additionally, we tested several subsets of each data set to ensure that the reconstruction parameters were optimized to provide uniform density in three dimensions and that this atomic density was consistent with the expectations for PbTe. Once a 3D reconstruction was obtained, the precipitates were clearly observed. Additionally, the precipitates could be delineated by generating an isoconcentration surface at 20–50% Ag.

References

[1] G.S. Nolas, J. Poon, M. Kanatzidis, MRS Bulletin 31 (2006) 199–205.
[2] M.S. Dresselhaus, G. Chen, M.Y. Tang, R.G. Yang, H. Lee, D.Z. Wang, Z.F. Ren, J.P. Fleurial, P. Gogna, Advanced Materials 19 (2007) 1043–1053.
[3] G.J. Snyder, E.S. Toberer, Nature Materials 7 (2008) 105–114.
[4] M.G. Kanatzidis, Chemistry of Materials 22 (2010) 648–659.
[5] L.D. Hicks, M.S. Dresselhaus, Physical Review B 47 (1993) 16631–16634.
[6] L.D. Hicks, M.S. Dresselhaus, Physical Review B 47 (1993) 12727–12731.
[7] S.V. Faleev, F. Leonard, Physical Review B 77 (2008) 214304.
[8] K.F. Hsu, S. Loo, F. Guo, W. Chen, J.S. Dyck, C. Uher, T. Hogan, E.K. Polychroniadis, M.G. Kanatzidis, Science 303 (2004) 818–821.
[9] J.P. Heremans, C.M. Thrush, D.T. Morelli, Journal of Applied Physics 98 (2005) 063703.
[10] W. Kim, J. Zide, A. Gossard, D. Klenov, S. Stemmer, A. Shakouri, A. Majumdar, Physical Review Letters 96 (2006) 045901.
[11] D.L. Medlin, G.J. Snyder, Current Opinion in Colloid & Interface Science 14 (2009) 226–235.
[12] T. Ikeda, L.A. Collins, V.A. Ravi, F.S. Gascoin, S.M. Haile, G.J. Snyder, Chemistry of Materials 19 (2007) 763–767.
[13] J.D. Sugar, D.L. Medlin, Journal of Alloys and Compounds 478 (2009) 75–82.
[14] J.R. Sootsman, J.Q. He, V.P. Dravid, C.P. Li, C. Uher, M.G. Kanatzidis, Journal of Applied Physics 105 (2009) 083718.
[15] Y. Gelbstein, B. Dado, O. Ben-Yehuda, Y. Sadia, Z. Dashevsky, M.P. Dariel, Chemistry of Materials 22 (2009) 1054–1058.
[16] S.S. Ragimov, S.A. Aliev, Inorganic Materials 43 (2007) 1184–1186.
[17] F. Drymiotis, T. Drye, D. Rhodes, Q. Zhang, J.C. Lashey, Y. Wang, S. Cawthorne, B. Ma, S. Lindsey, T. Tritt, Journal of Physics-Condensed Matter 22 (2010) 035801.
[18] J. Androulakis, K.F. Hsu, R. Pcionek, H. Kong, C. Uher, J.J. Dangelo, A. Downey, T. Hogan, M.G. Kanatzidis, Advanced Materials 18 (2006) 1170–1173.
[19] M. Zhou, J.F. Li, T. Kita, Journal of the American Chemical Society 130 (2008) 4527–4532.
[20] E. Quarez, K.F. Hsu, R. Pcionek, N. Frangis, E.K. Polychroniadis, M.G. Kanatzidis, Journal of the American Chemical Society 127 (2005) 9177–9190.
[21] L.J. Wu, J.C. Zheng, J. Zhou, Q. Li, J.H. Yang, Y.M. Zhu, Journal of Applied Physics 105 (2009) 094317.
[22] A.L. Dawar, S.K. Paradkar, P. Kumar, O.P. Taneja, P.C. Mathur, Physica Status Solidi A-Applied Research 68 (1981) 227–232.
[23] F.J. Bryant, D.M. Staudte, Radiation Effects and Defects in Solids 62 (1982) 69–75.
[24] M. Orihashi, Y. Noda, T.H. Kaibe, I.A. Nishida, Journal of the Japan Institute of Metals 61 (1997) 241–246.
[25] K. Ahn, C.P. Li, C. Uher, M.G. Kanatzidis, Chemistry of Materials 21 (2009) 1361–1367.
[26] F. Wald, Journal of the Less-Common Metals 13 (1967) 579–590.
[27] R. Blachnik, B. Gather, Journal of the Less-Common Metals 60 (1978) 25–32.
[28] Y. Noda, S. Ohba, S. Sato, Y. Saito, Acta Crystallographica Section B-Structural Science 39 (1983) 312–317.
[29] C. Manolikas, Journal of Solid State Chemistry 66 (1987) 1–6.
[30] P. Rahlfs, Z. Phys. Chem. B-Chem. Elem. Aufbau. Mater. 31 (1936) 157–194.
[31] A.J. Frueh, Acta Crystallographica 13 (1960) 1007–11007.
[32] A.J. Frueh, American Mineralogist 46 (1961) 654–660.
[33] T.F. Kelly, M.K. Miller, Review of Scientific Instruments 78 (2007) 031101.
[34] D.N. Seidman, Annual Review of Materials Research 37 (2007) 127–158.
[35] G.B. Thompson, M.K. Miller, H.L. Fraser, Ultramicroscopy 100 (2004) 25–34.
[36] M.K. Miller, K.F. Russell, G.B. Thompson, Ultramicroscopy 102 (2005) 287–298.
[37] E.R. Weibel, Stereological Methods, vol. 2, Academic Press, London, 1980.
[38] T. Ikeda, S.M. Haile, V.A. Ravi, H. Azizgolshani, F. Gascoin, G.J. Snyder, Acta Materialia 55 (2007) 1227–1239.
[39] R. Dalven, Infrared Physics 9 (1969) 141–184.
[40] J.L. Cui, X.B. Zhao, Materials Letters 57 (2003) 2466–2471.
[41] J. Schneider, H. Schulz, Zeitschrift fur Kristallographie 203 (1993) 1–15.
[42] B. Houston, R.E. Strakna, H.S. Belson, Journal of Applied Physics 39 (1968) 3913–3916.
[43] B.A. Parker, D.R.F. West, Journal of the Australasian Institute of Metals 14 (1969) 102–110.
[44] E.P. Butler, G. Thomas, Acta Metallurgica 18 (1970) 347–365.
[45] A.G. Khachaturyan, S.V. Semenovskaya, J.W. Morris, Acta Metallurgica 36 (1988) 1563–1572.
[46] F.R.N. Nabarro, Proceedings of the Physical Society 52 (1940) 90–93.
[47] M.E. Thompson, C.S. Su, P.W. Voorhees, Acta Metallurgica et Materialia 42 (1994) 2107–2122.
[48] M.E. Thompson, P.W. Voorhees, Acta Materialia 47 (1999) 983–996.
[49] F. Ren, E.D. Case, J.R. Sootsman, M.G. Kanatzidis, H.J. Kong, C. Uher, E. Lara-Curzio, R.M. Trejo, Acta Materialia 56 (2008) 5954–5963.
[50] H. Khachai, R. Khenata, A. Bouhemadou, A.H. Reshak, A. Haddou, M. Rabah, B. Soudini, Solid State Communications 147 (2008) 178–182.
[51] R. Leitsmann, L.E. Ramos, F. Bechstedt, Physical Review B 74 (2006).
[52] A.J. Ardell, Metallurgical Transactions 1 (1970) 525–534.
[53] A.J. Ardell, Acta Metallurgica 20 (1972) 61–71.
[54] J.W. Christian, The Theory of Transformations in Metals and Alloys, third ed., Pergamon, Oxford, 2002.
[55] J.P. Hirth, X.X. Feng, Journal of Applied Physics 67 (1990) 3343–3349.
[56] J.W. Matthews, A.E. Blakeslee, Journal of Crystal Growth 27 (1974) 118–125.